nature energy

Article

https://doi.org/10.1038/s41560-023-01272-1

Roll-to-roll prelithiation of lithium-ion battery anodes by transfer printing

Received: 31 August 2022

Accepted: 9 May 2023

Published online: 8 June 2023

Check for updates

Cheng Yang[1,2,7], Huachun Ma[2,7], Ruichuan Yuan[1], Kuangyu Wang[1], Kai Liu[3], Yuanzheng Long[1], Fei Xu[4], Lei Li[5], Haitian Zhang[6], Yingchuan Zhang[1], Xiaoyan Li[2] ✉ & Hui Wu[1] ✉

Prelithiation can boost the performance of lithium-ion batteries (LIBs). A cost-effective prelithiation strategy with high quality and high industrial compatibility is urgently required. Herein we developed a roll-to-roll electrodeposition and transfer-printing system for continuous prelithiation of LIB anodes. By roll-to-roll calendering, pre-manufactured anodes could be fully transfer-printed onto electrodeposited lithium metal. The interface separation and adhesion during transfer printing were related to interfacial shear and compressive stress, respectively. With the facile transfer-printing prelithiation, high initial Coulombic efficiencies of 99.99% and 99.05% were achieved in graphite and silicon/carbon composite electrode half cells, respectively. The initial Coulombic efficiencies and energy densities in full cells were observed to be significantly improved with the prelithiated electrodes. The roll-to-roll transfer printing provides a high-performance, controllable, scalable and industry-adaptable prelithiation in LIBs.

Despite intensive study and rapid progress in the field of lithium-ion batteries (LIBs), the widespread transitions to electric vehicles are being restricted by the limited driving ranges, which are constrained by the energy density of the LIBs[1–3]. Further enhancement of energy density of LIBs has been a critical and challenging research area in the past decade[4,5]. For a LIB, the formation of solid electrolyte interphase (SEI) on the anode consumes a large amount of lithium ions and results in a low initial Coulombic efficiency (ICE) and severe decay of energy density[6]. For example, 5–15% of the capacity of a LIB from the cathode is consumed in these reactions when a commercial graphite anode is used[7]. Moreover, for the next-generation high-energy-density silicon-based anodes, the lithium loss could more severely impair the energy density due to the increase in the superficial area of formed SEI in nanostructured silicon anodes[8,9]. During the past decade, prelithiation has been recognized as an effective way to address the issue of active lithium loss and improve the energy density of next-generation LIBs. To date, various prelithiation methods have been developed based on different mechanisms[8–10]. Prelithiation strategies introduce extra active lithium ions through various lithium sources, and these extra lithium ions contribute to the formation of SEI, eventually resulting in improvement of energy density[11].

Stabilized lithium metal powder has been intensively studied as an additive for prelithiation to react with anode active materials after electrolyte infiltration during battery assembly[12–14]. It has been proven to be a simple and direct prelithiation strategy that is suitable for large-scale production[12,14]. However, this method suffers from high costs during the production and dispersion of stabilized lithium metal powder[11]. Other disadvantages of this method include the potential safety hazard of the reactive Li powders and the large-scale usage of toxic and harmful solvents such as methylbenzene to disperse the Li powders. Addition of a piece of lithium metal foil on the anode is another common approach for anode prelithiation[15–17]. In a commercial

[1]State Key Laboratory of New Ceramics and Fine Processing, School of Materials Science and Engineering, Tsinghua University, Beijing, China. [2]Center for Advanced Mechanics and Materials, Applied Mechanics Laboratory, Department of Engineering Mechanics, Tsinghua University, Beijing, China. [3]State Key Laboratory of Alternate Electrical Power System with Renewable Energy Sources, School of New Energy, North China Electric Power University, Beijing, China. [4]Do-Fluoride New Energy Technology Co. Ltd., Jiaozuo, China. [5]National Engineering Research Center of Electric Vehicles, Beijing Institute of Technology, Beijing, China. [6]Institute of Nuclear and New Energy Technology, Tsinghua University, Beijing, China. [7]These authors contributed equally: Cheng Yang, Huachun Ma. ✉e-mail: xiaoyanlithu@tsinghua.edu.cn; huiwu@tsinghua.edu.cn

LIB, the loss of active lithium is below 1 mAh cm^{-2}, which indicates that an extremely thin lithium metal foil (thickness <5 μm) is required for an accurate lithium compensation[15]. However, self-supporting lithium metal foil with thickness below 20 μm is beyond the reach of traditional extrusion technologies because of their mechanical fragility[15]. Electrochemical approaches implemented through galvanostatic charge–discharge or short circuiting with a sacrificial anode also constitute a potential choice for scaled-up production of prelithiation anodes[18–20]. These strategies could precisely adjust the lithiation degree of anodes[9,11]. Nevertheless, they require a temporary half cell or a complicated reassembling process[9]. Moreover, the anodes have to be cleaned and reassembled after the immersion in the electrolyte of the LIB. Furthermore, the prelithiation process is time consuming due to the restricted applied current[18]. Chemical prelithiation performed by immersing the anode in lithium-containing solutions (such as lithium-bipheny/tetrahydrofuran, lithium-naphthalene/methoxymethane) is also a promising method[21–23]. However, typical prelithiation solutions fail to react with graphite anodes due to their higher redox potential than graphite[21]. Besides, immersing the anodes in organic solvents such as tetrahydrofuran or methoxymethane may result in the adhesive failure of certain binders. As a result, unfortunately both the electrochemical and chemical prelithiation methods are hard to link with currently used roll-to-roll process battery assembly. A few attempts have been made to combine prelithiation with roll-to-roll process[18,24–26]. However, these methods are limited by their complexity, low feasibility or lack of universality. Therefore, a cost-effective, controllable and industry-adaptable method for anode prelithiation is long awaited and urgently required.

Herein a transfer-printing prelithiation method was designed. By optimizing the electrodeposition parameters, a controlled amount of lithium was deposited on current collectors. Taking advantage of the strong bonding force between the deposited lithium and anode layer, an electrode transfer-printing process was employed to transfer the active material onto the electrode. With this method, prelithiated graphite and silicon/carbon (Si/C) composite anodes were successfully prepared. Both anodes exhibited improved ICEs (99.99% and 99.05%, respectively) with stable cyclabilities. The prelithiated electrodes led to efficient improvement of the ICEs and energy densities of $Li(NiCoMn)_{1/3}O_2$ (NCM) and $LiFePO_4$ (LFP) full cells. Both the kinematic details and underlying mechanisms of the transfer-printing process were further revealed via finite element (FE) modelling. On this basis, a roll-to-roll electrodeposition and transfer-printing (RET) system was designed for continuous production of prelithiated anodes. A continuous production process from current collector to prelithiated anodes was achieved, which can well match with the conventional roll-to-roll battery manufacturing process.

Fabrication and characterization of prelithiated electrodes

Figure 1a shows the schematic illustration of the fabrication of our single-sided prelithiated graphite (preGr) electrode. First, a common graphite coating was prepared on a smooth stainless-steel surface by slurry coating, and then, a thin lithium layer was deposited on a copper foil by electrodeposition. Finally, the lithium-coated copper foil (LiCF) was calendered with the graphite-coated stainless steel (GrSS) to transfer the graphite layer onto the copper foil. Supplementary Fig. 1a–d demonstrates the photograph of the preGr anode, LiCF, GrSS and GrSS after transfer printing, revealing that an intact area of graphite layer is peeled off from the GrSS and transferred onto LiCF. Supplementary Fig. 2a–c shows the cross-section scanning electron microscopy (SEM) images and energy-dispersive X-ray spectroscopy (EDS) images of LiCF and GrSS. Compared with common electrochemical prelithiation methods, a much higher current density (up to 10 mA cm^{-2}) can be applied in our transfer-printing method, thus allowing a higher producing speed (Supplementary Fig. 3). In our prelithiated electrode, the copper layer works as a current collector, and the graphite layer serves as an active material. The lithium layer is designed as a lithium source for prelithiation reaction.

For a better match with the lithium loss in graphite electrodes, the capacity of deposited lithium was precisely adjusted to achieve an ICE of approximately 100%. By transfer printing, graphite anodes with lithium-loading equivalent to 30% of the graphite capacity (372 mAh g^{-1}) were prepared (the electrode is noted as 30 preGr electrode). Figure 1b–g shows the cross-sectional SEM images of the 30 preGr electrode and Gr electrode. The thickness of both electrodes was about 30 μm. After the transfer-printing process, the 60 μm-thick pristine Gr layer on stainless steel was compressed down to about 20 μm on the preGr anode (Fig. 1b and Supplementary Fig. 2c). The closely connected interfaces between these layers can be confirmed by magnified SEM image and the lithium layer of 30 preGr is about 2 μm (Fig. 1c). The EDS image of 30 preGr (Fig. 1d) shows a clear separation of carbon, oxygen and copper signals, which demonstrates the three-tier structure of the preGr anode. An SEI layer was formed on the deposited lithium during the lithium deposition, thus the lithium layer displays obvious signals corresponding to oxygen. In contrast, there is no platelike oxygen signal in the EDS images of the Gr anode (Fig. 1g). Supplementary Fig. 4a,b displays the surface details of Gr and 30 preGr anodes. PreGr anodes produced by the transfer-printing process with different loads of lithium metal present similar three-tier structures as indicated by cross-sectional SEM images (Supplementary Fig. 5a,b). Supplementary Fig. 6 shows the sectional-view SEM images of 30 preGr electrode after the prelithiation reaction.

Prelithiation of graphite and Si/C anodes for full cells

For further investigation of the prelithiation reaction, a series of preGr (30 preGr, 100 preGr, 200 preGr and 300 preGr) anodes with different amounts of electrodeposited lithium were prepared through the method mentioned above and assembled in C2025 cells. After a static stage of 24 h, the graphite layer of the preGr anode underwent a complete reaction with active lithium with the intervention of electrolyte to form lithium–graphite intercalation compounds (Li–GICs) with different compositions (Supplementary Fig. 7). Compared with pristine Gr anodes, these preGr anodes exhibit gradual colour variation from black to gold, indicating the formation of golden LiC_6 compounds in the 200 preGr anode and 300 preGr anode (Fig. 2a).

Moreover, X-ray diffraction (XRD) patterns and Raman spectra were provided for further understanding the chemical changes occurring in these preGr anodes (Fig. 2b,c). With the augment of active lithium, several new peaks are detected, reflecting the evolution of Li–GICs[27–29]. Peaks at 26.4°, 25.3° and 24.0° are recognized as {002} peak of graphite, {002} peak of LiC_{12} and {001} peak of LiC_6, respectively. Moreover, peaks at $2\theta = 25.7°$ and $2\theta = 26.2°$ are correlated with the appearance of Li–GICs with low levels of lithium insertion[29]. Clearly, after the prelithiation reaction, 30 preGr consists of a mixture of graphite and Li–GICs with low levels of lithium insertion[27]. With the increased active lithium in preGr electrodes, LiC_{12} begins to emerge in 100 preGr and 200 preGr. Finally, Li–GICs in the 300 preGr anode are all made up of LiC_6. The lithium intercalation process in the preGr electrodes was also verified by Raman spectroscopy (Fig. 2c). For the 30 preGr and 100 preGr anodes, the G-band line gradually shifts up from the original graphite line and sharpens, representing low levels of Li insertion[30]. For the 200 preGr electrode, two new lines appear at both sides of the original graphite lines, which are assigned to the appearance of LiC_{12} (ref. 30). Finally, the original G-band line gets completely vanished for 300 preGr anodes, revealing the entire lithiation of graphite[30]. Supplementary Fig. 8 displays the X-ray photoelectron spectroscopy (XPS) results of Gr and 30 preGr electrodes after prelithiation reaction. Evidently, an increase in 30 preGr O 1*s* branches occurs compared to Gr, indicating the formation of oxygen-containing SEI compounds on

https://doi.org/10.1038/s41560-023-01272-1

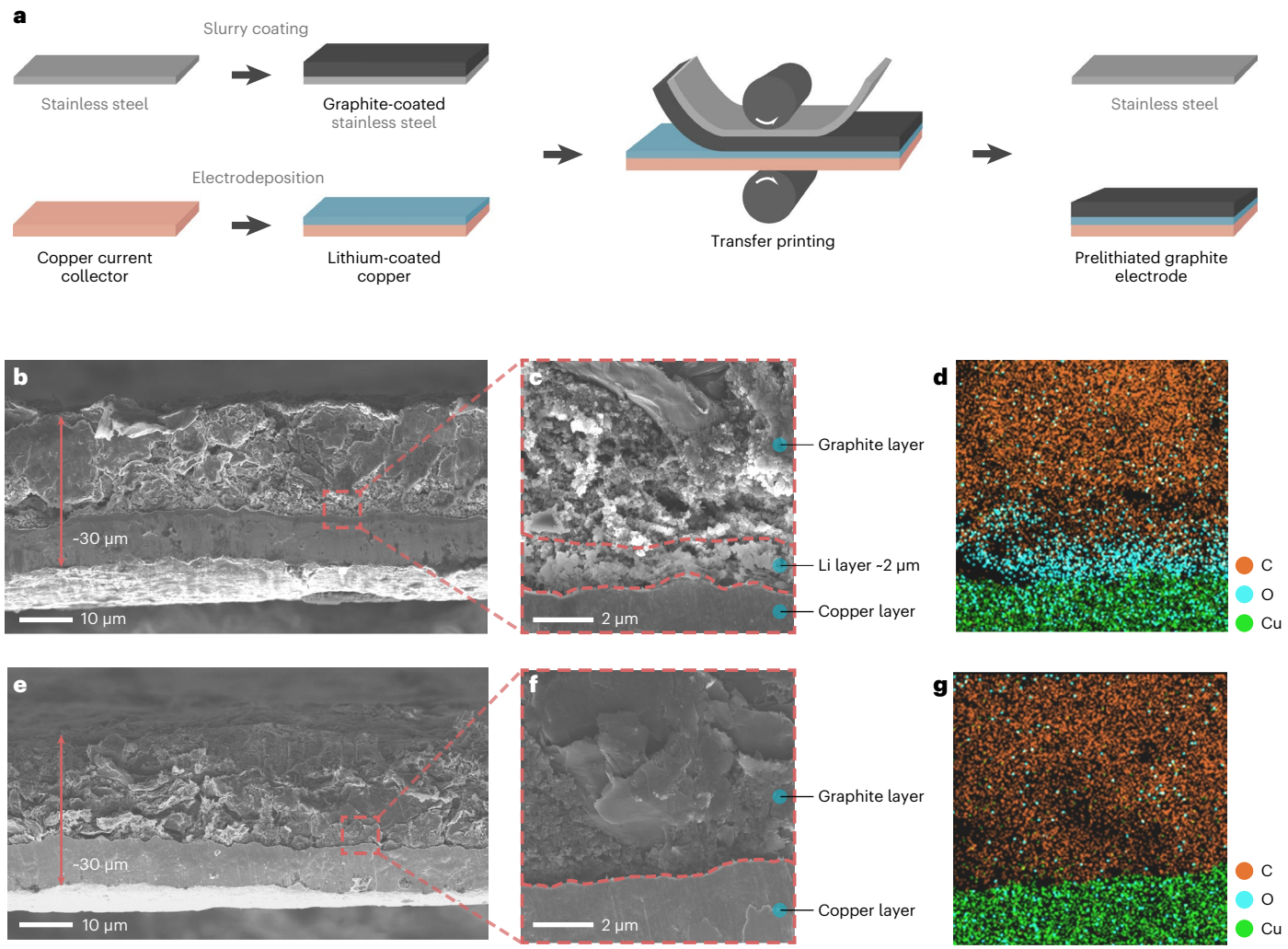

Fig. 1 | Fabrication of single-sided preGr electrode. a, Schematic illustration of the fabrication of our single-sided preGr electrode. Stainless steel is light grey, graphite is dark grey, copper is brown and lithium is blue. **b**,**c**, Cross-sectional SEM images of preGr electrodes. **d**, EDS image of preGr electrodes. **e**,**f**, Cross-sectional SEM images of Gr electrodes. **g**, EDS image of Gr electrodes.

the surface. After prelithiation, a new peak at 288.8 eV correlated with lithium carbonate or lithium alkyl carbonates (O–C=O) in C 1*s* spectra confirms the SEI formation, and similarly, a new peak at 684.8 eV in F 1*s* spectra is assigned to lithium fluoride[31]. In the case of Li 1*s* spectra, the new peak at 55.5 eV is likely to merge from subpeaks correlated with lithium fluoride, lithium carbonate, lithium alkyl carbonates and Li–GIC compounds.

Noteworthy, proper prelithiation followed by the method proposed in this study can fully recover the lithium loss in the first cycle. Without prelithiation, an artificial graphite anode displays a relatively low ICE of 83.13% in Gr||Li half cells (Fig. 2d) with a lithium loss of 69.7 mAh g^{-1} in the first charge–discharge cycle. In contrast, in a 30 preGr||Li half cell, the ICE increases up to 99.99% and a decrease of open-circuit voltage (OCV) from 2.427 to 0.3702 V is observed (Fig. 2d). For further investigation, a delithiation test of 30 preGr anode was carried out in a preGr||Li half cell (Fig. 2e), and 30 preGr anode exhibits a delithiation capacity of 22.94 mAh g^{-1} and the capacity of electrodeposited lithium is 111.6 mAh g^{-1}. It indicates that not only SEI compounds, but also certain amounts of Li–GICs are formed after the prelithiation reaction in 30 preGr. The voltage profiles of Gr||Li half cells show an obvious voltage platform of SEI formation at about 1.0 V in the first cycle compared with that in the second (Supplementary Fig. 9).

More details are presented by analysing cyclic voltammetry (CV) curves of Gr and 30 preGr anodes (Fig. 2f). The two anodes share a similar pattern, that is, a reduction slope from 0.5 to 0 V and a single oxidation peak at about 0.35 V. However, the Gr anodes own another reduction peak at about 1.0 V due to the SEI formation at the surface of electrodes. Furthermore, a larger increase at the oxidation peak in subsequent scans reveals a worse reversibility compared to the 30 preGr anode. Thus, beneficially, a higher Coulombic efficiency in the first five cycles is achieved in Gr||Li half cells by using the 30 preGr electrode, indicating the formation of an SEI with higher cycling efficiency (Supplementary Fig. 10). Supplementary Fig. 11 illustrates the differential capacity (dQ/dV) plots of Gr and 30 preGr electrodes at the first lithiation process. The peaks appearing at 0.20, 0.11 and 0.07 V are correlated with different lithiation stages. Compared with the Gr electrode, the 30 preGr electrode exhibits a weaker peak at 0.20 V, indicating the insertion of lithium ions. Moreover, a peak of Gr anode is detected at 1.0 V, which is supposed to be corresponding to the SEI formation.

With the gradual increase of lithium loading, the OCVs of these cells sharply decline and the ICEs steadily increase (Fig. 3a). The lithium-loading capacity of each preGr anode can be carefully controlled by electrodeposition parameters, and notably, preGr anodes

https://doi.org/10.1038/s41560-023-01272-1

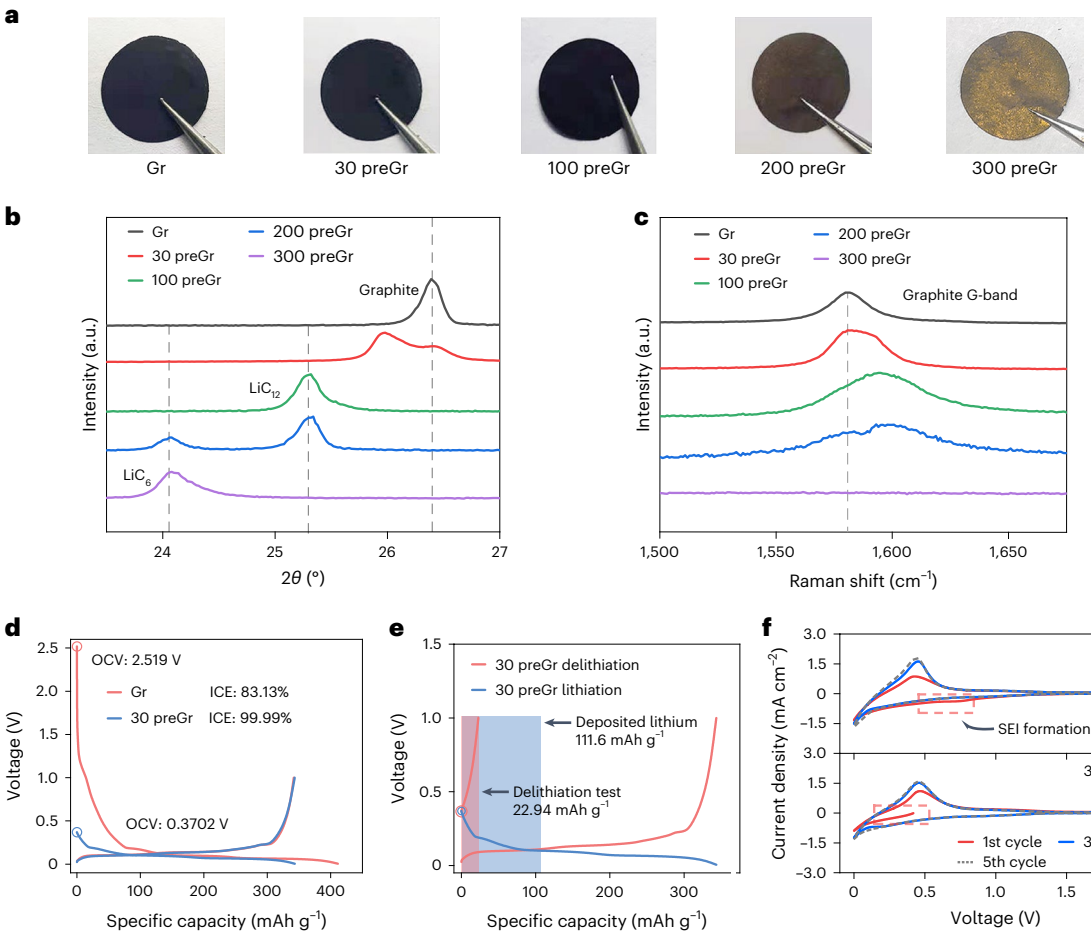

Fig. 2 | Characterizations of preGr electrodes. a, Photographs of Gr, 30 preGr, 100 preGr, 200 preGr and 300 prGr electrodes. **b**, XRD patterns of Gr, 30 preGr, 100 preGr, 200 preGr and 300 prGr electrodes. **c**, Raman spectra of Gr, 30 preGr, 100 preGr, 200 preGr and 300 prGr electrodes. **d**, Voltage profiles of the Gr and 30 preGr electrodes. The open-circuit voltage (OCV) of these cells is presented. **e**, Delithiation test of the 30 preGr electrode and the capacity comparison with deposited lithium. **f**, CV curves of Gr and 30 preGr anodes.

with the same lithium loading maintain good consistency in different batches (Fig. 3b). In a full cell, excessive lithium-ion compensation results in harmful lithium plating on the anode surface, leading to unfavourable weak battery performance and potential safety hazards. Consequently, the stable and controllable lithium-ion compensation ability of preGr anodes designed in this study is of great importance for prelithiated electrodes. Electrochemical impedance spectroscopy (EIS) was used to monitor the evolution of SEI of Gr and 30 preGr half cells during cycles (Fig. 3c and Supplementary Fig. 12). R_0 represents the ohmic conductor; R_{CC} represents the conduction behaviour between electrodes and current collector; and R_{SEI} represents the influences of SEI[32]. Clearly, the results indicate that the 30 preGr anode has a lower R_{SEI} during cycling. The above-mentioned phenomenon demonstrates that 30 preGr electrodes own a better SEI for lithiation reaction during the first cycles.

The cycling performance of the Gr and the 30 preGr electrodes is displayed in Fig. 3d. For achieving better performance of these cells, they were first activated at 0.1C (1C = 372 mAh g^{-1}) for ten cycles and then run at 0.5C for 140 cycles. The initial delithiation capacities of 30 preGr and Gr electrodes are 317.7 and 304.4 mAh g^{-1}, respectively, at the first cycle of 0.5C, and after 140 cycles, the capacity changes to 341.4 and 333.4 mAh g^{-1}, respectively. The capacity retentions of these electrodes are 107% and 110%, respectively. After prelithiation, the 30 preGr anode exhibits no drawback in cycling stability compared to Gr anodes. Figure 3e further evaluates the rate capabilities of the Gr and the 30 preGr anodes at current rates of 0.1C, 0.2C, 0.5C and 1C. During the test, the 30 preGr electrodes reveal gradually decreasing capacities of 348.3, 338.3, 320.7 and 266.7 mAh g^{-1}, respectively, and show a better rate capability compared to the Gr anode at all rates.

Notably, the transfer-printing process is also an ideal choice for the prelithiation of other active anode materials. Commercial Si/C material with a capacity of about 450 mAh g^{-1} was used as an example (Supplementary Fig. 13). Prelithiated Si/C (preSi/C) anodes with a lithium-loading equivalent of 25% of the Si/C capacity (25 preSi/C anodes) were fabricated. Figure 3f shows the cross-sectional SEM image of the 25 preSi/C anodes, which share a similar three-tier structure with preGr anodes. Without prelithiation, the Si/C anode displays an ICE of 85.37% in half cells (Fig. 3g). For cells with the 25 preSi/C anodes, the ICE increases up to 99.05% with a decrease of OCV from 2.351 to 0.2995 V (Fig. 3g). Supplementary Fig. 14a,b shows the CV and EIS features of Si/C and 25 preSi/C electrodes. Further testing shows the absence of obvious capacity fading in 25 preSi/C anode half cells during a long cycling test (Fig. 3h). The successful prelithiation of artificial graphite materials and Si/C materials demonstrates the wide applicability as an anode prelithiation method for LIBs.

NCM and LFP full cells were produced for practical evaluation of the preGr and preSi/C anodes with an NP ratio of 1.1. Compared with the Gr||NCM full cell, the ICE of the 30 preGr||NCM cell improves from 83.10% to 89.39% and a higher reversible capacity of 153.3 mAh g^{-1} at 0.1C (1C = 200 mAh g^{-1}) is delivered (Fig. 4a and Supplementary Fig. 15).

https://doi.org/10.1038/s41560-023-01272-1

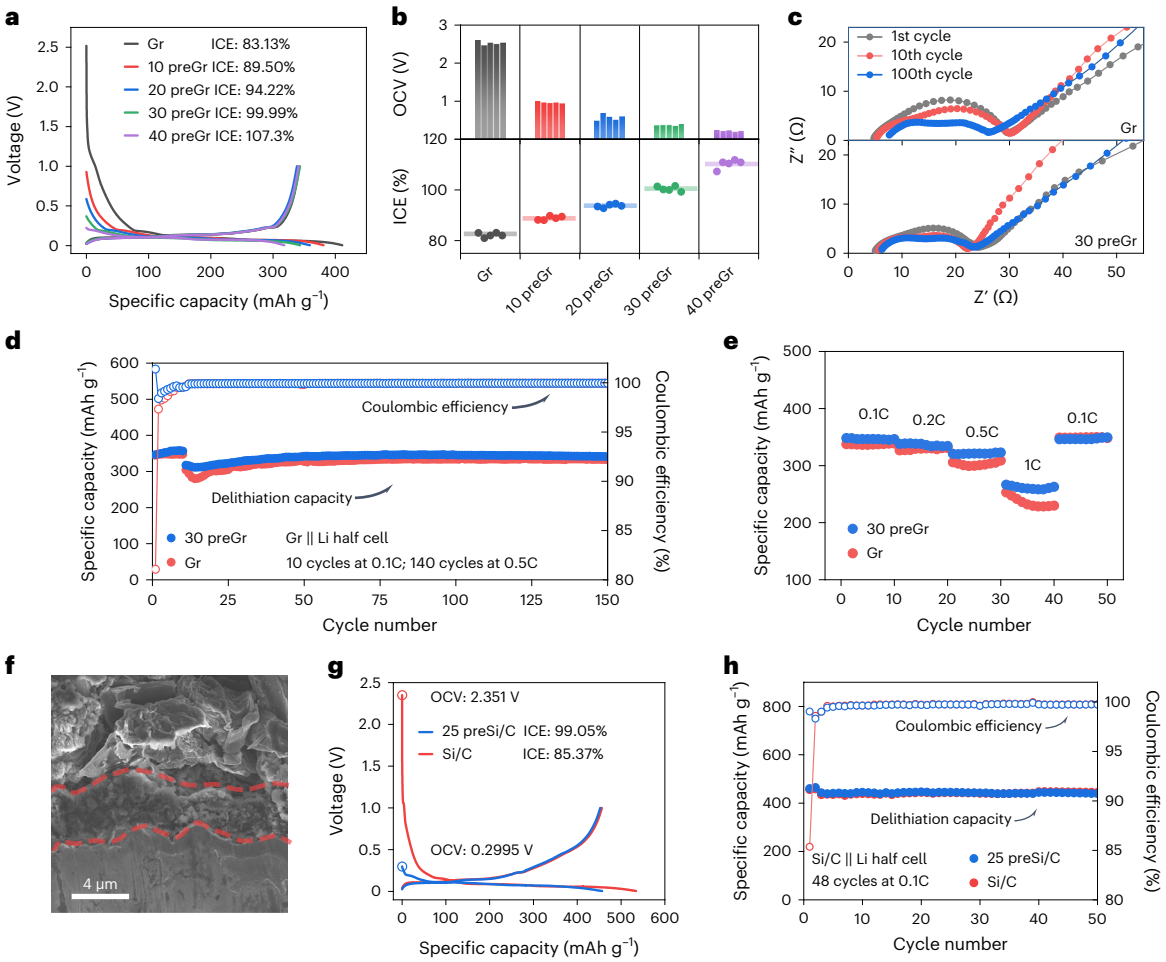

Fig. 3 | Electrochemistry features of preGr and preSi/C electrodes. **a**, Voltage profiles of the Gr, 10 preGr, 20 preGr, 30 preGr and 40 preGr electrodes. **b**, Comparisons of the OCVs and ICEs of multiple graphite electrodes with different lithiation capacities. **c**, Equivalent circuits of the Gr and 30 preGr half cells after 1, 10 and 100 cycles. **d**, Galvanostatic cycling of Gr and 30 preGr half cells. For these cells, 1C = 372 mAh g^{-1}. **e**, Rate capacity of Gr and 30 preGr half cells at various current rates. **f**, Cross-sectional SEM image of 25 preSi/C anodes. **g**, Voltage profiles of the Si/C and 25 preSi/C electrodes. **h**, Galvanostatic cycling of Si/C and 25 preSi/C half cells. For these cells, 1C = 450 mAh g^{-1}.

The 30 preGr||NCM cell achieves a discharge capacity retention of 79.6% and a capacity advantage of about 10 mAh g^{-1} after 595 cycles at 0.5C (Fig. 4b). At a high rate of 1.5C, the 30 preGr||NCM cell achieves a discharge capacity retention of 76.1% and a capacity advantage of about 30 mAh g^{-1} after 1,000 cycles (Supplementary Fig. 16). Full cells with anodes of 20 preGr and 40 preGr and full cells with NP ratio of 1.0 and 1.2 are also assembled and compared (Supplementary Figs. 17 and 18). In these comparisons, the 30 preGr cell exhibited both energy density and safety advantages. For the LFP cathode, the ICE of the 30 preGr||LFP cell improves from 79.91% to 95.88% and a higher reversible capacity of 153.4 mAh g^{-1} at 0.1C (1C = 170 mAh g^{-1}) is delivered (Fig. 4c and Supplementary Fig. 19). The 30 preGr||LFP cell achieves a discharge capacity retention of 99.8% and a capacity advantage of about 28 mAh g^{-1} after 195 cycles at 0.5C (Fig. 4d). The energy densities of the 30 preGr||NCM and the 30 preGr||LFP cell improve from 363.8 to 380.2 Wh kg^{-1} and 264.7 to 329.6 Wh kg^{-1}, respectively (Fig. 4e). The higher improvements of energy densities (28 mAh g^{-1} compared to 11 mAh g^{-1}) and ICE (6% compared to 16%) in LFP full cells originate from the high ICE of LFP half cells (Supplementary Fig. 20). Comparative analysis indicates that the ICEs of LFP and NCM half cells are measured as 90.17% and 96.86% (Supplementary Figs. 21 and 22). In the 25 preSi/C||NCM full cell, the ICE increases from 83.04% to 89.21%, and the reversible capacity increases to 149.8 mAh g^{-1} at 0.05 C (1C = 200 mAh g^{-1}) (Fig. 4f). The 25 preSi/C||NCM cell achieves a discharge capacity retention of 95.1% and a capacity advantage of about 23 mAh g^{-1} after 98 cycles at 0.1C (Fig. 4g). The energy density of the 25 preSiC||NCM cell also improves from 375.8 to 401.5 Wh kg^{-1} (Fig. 4h).

Transfer-printing mechanisms

To reveal both the kinematic details and underlying mechanisms of transfer printing in the roll-to-roll fabrication, a series of FE simulations were performed for rolling depressions of the prelithiated anode. The mixed-mode cohesive zone model was used in these simulations to describe the separation and adhesion behaviours of interfaces. The parameters of cohesive zone model used in our simulations were obtained from a 90° peeling experiment (Supplementary Figs. 23 and 24). Typical curves of energy release rate vs peeling distance of GrSS samples and prelithiated electrodes were measured and presented in Supplementary Figs. 25 and 26. Details of the FE simulations and peeling experiments are given in Supplementary Note 1 (Supplementary Figs. 25–27 and Supplementary Table 1). Figure 5a illustrates that the simulated system consists of two rollers with a diameter of 5 cm, the LiCF with layer thickness of 13 μm and the GrSS with layer thickness of 75 μm. All the set-ups of these simulations were consistent with experiments. Figure 5b shows the shear stress distributions of LiCF and GrSS. Due to the difference in shear modulus between LiCF and

https://doi.org/10.1038/s41560-023-01272-1

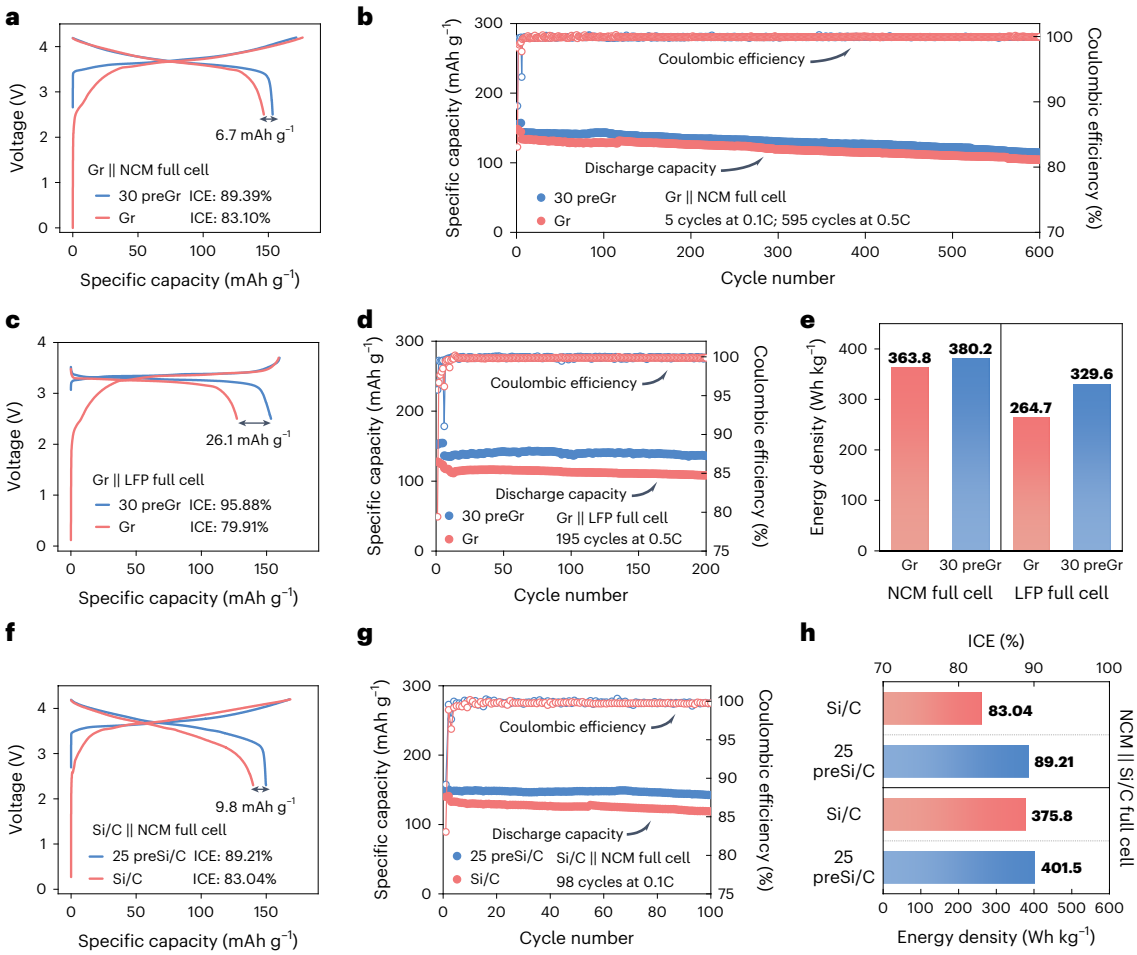

Fig. 4 | ICE improvements and cycling stabilities of prelithiated full cells. **a**, Voltage profiles of the Gr||NCM and 30 preGr||NCM full cells. **b**, Galvanostatic cycling of the Gr||NCM and 30 preGr||NCM full cells. For these cells, 1C = 200 mAh g^{-1} based on cathodes. **c**, Voltage profiles of the Gr||LFP and 30 preGr||LFP full cells. **d**, Galvanostatic cycling of the Gr||LFP and 30 preGr||LFP full cells. For these cells, 1C = 170 mAh g^{-1} based on cathodes. **e**, Comparisons of the energy densities of the NCM and LFP full cells. **f**, Voltage profiles of the Si/C||NCM and 25 preSi/C||NCM full cells. **g**, Galvanostatic cycling of the Si/C||NCM and 25 preSi/C||NCM full cells. For these cells, 1C = 200 mAh g^{-1} based on cathodes. **h**, Comparisons of the ICEs and energy densities of Si/C||NCM and 25 preSi/C||NCM full cells.

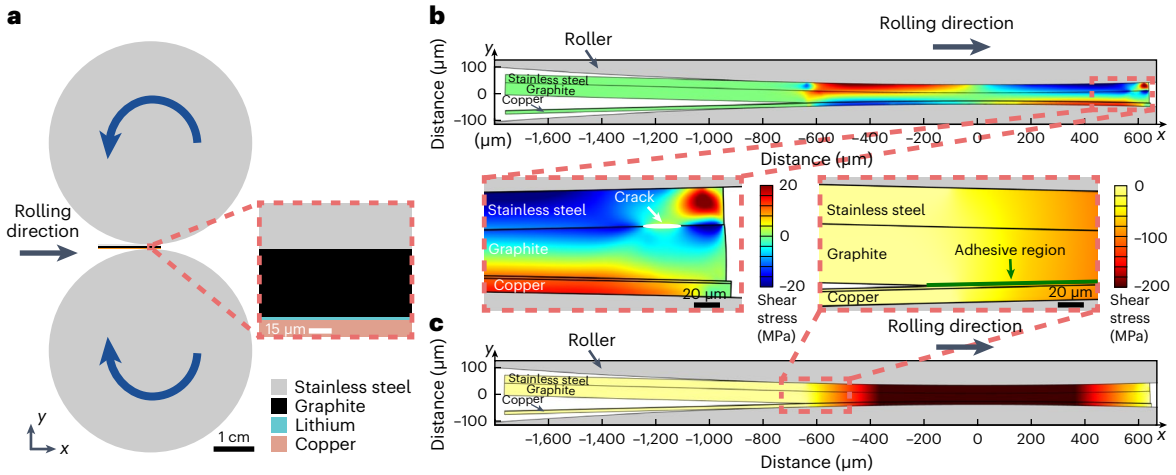

Fig. 5 | FE simulations for rolling depression of the prelithiated anode. **a**, FE model of two rollers, the LiCF and the GrSS. **b**, Shear stress of the LiCF and the GrSS with a compressive strain of 0.20. A crack marked in the inset indicates the initiation of separation between the stainless-steel and graphite layers. **c**, Pressure of the LiCF and the GrSS with a compressive strain of 0.20. An adhesive region marked in the inset indicates the initiation of adhesion between the graphite layer and lithium layer.

https://doi.org/10.1038/s41560-023-01272-1

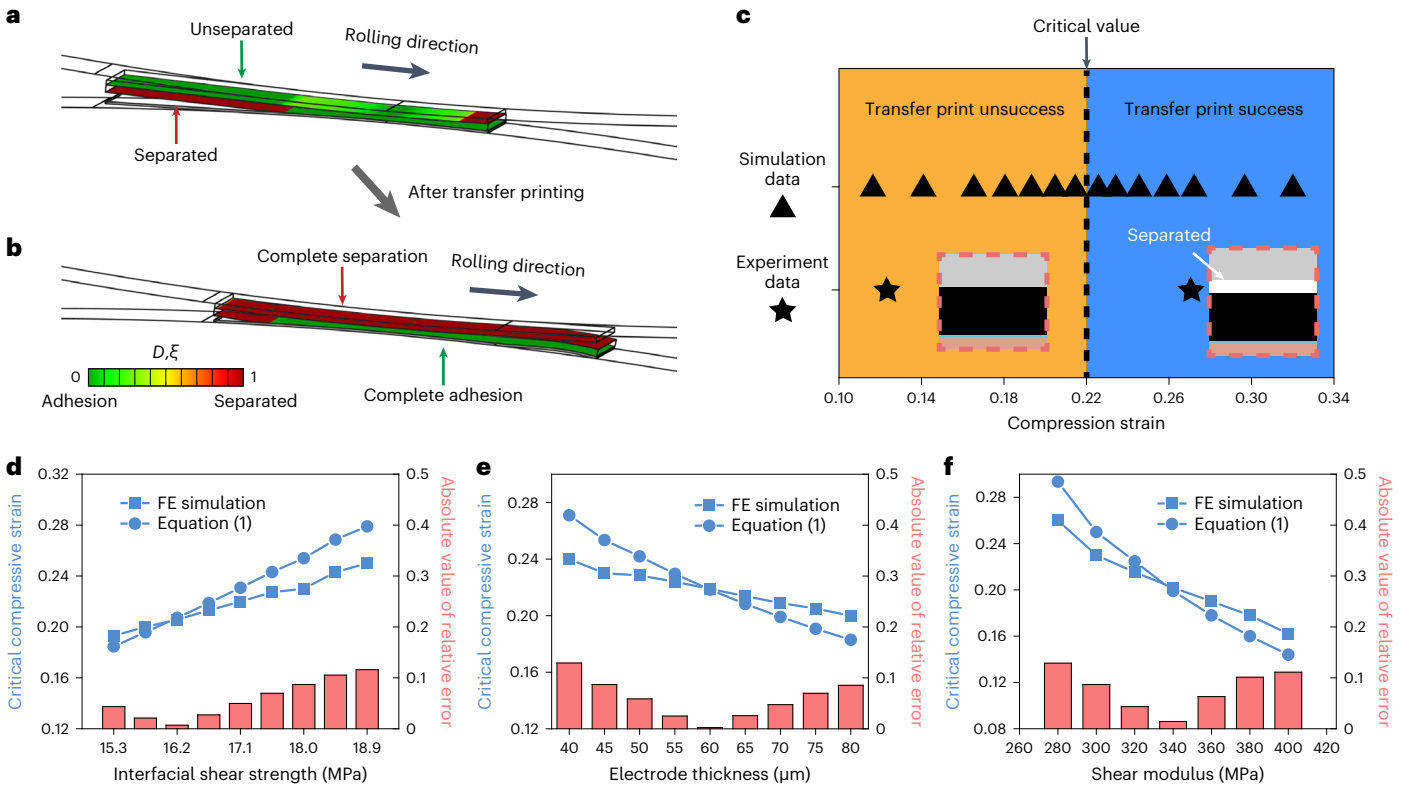

Fig. 6 | Tracking and simulations of interface separation and adhesion. a, Interface separation and adhesion during the transfer-printing process with a compressive strain of 0.23 and the roller rotation angle of 0. **b**, Interface separation and adhesion during the transfer-printing process with a compressive strain of 0.23 and the roller rotation angle of 0.03. **c**, Phase diagram of transfer printing based on the compressive strain. **d**, Comparison of critical compressive strains in the case of different interfacial shear strengths between FE simulation and the theoretical model. **e**, Comparison of critical compressive strains in the case of different electrode thicknesses between FE simulation and the theoretical model. **f**, Comparison of critical compressive strains in the case of different electrode shear moduli between FE simulation and the theoretical model.

GrSS, high shear stress is generated at the interfaces to maintain the strain compatibility during transfer printing. As shown in the inset in Fig. 5b, the shear stress at the interface between stainless-steel foils and graphite is up to about 20 MPa. On the basis of the Griffith's fracture theory, when the energy release rate driven by a high shear stress exceeds a critical value, the stainless-steel foil is separated from the graphite layer, indicating a mode II interface fracture[33]. As shown in Fig. 5c, the normal stress induced by vertical deformation is the compressive stress, making LiCF and GrSS contact with each other and further facilitating the adhesion between the graphite layer and lithium layer in the roll-to-roll fabrication.

To track the separation and adhesion behaviours during the transfer-printing process, two damage variables D ($D = 0$, no separation, and $D = 1$, complete separation) and ξ ($\xi = 1$, no adhesion, and $\xi = 0$, complete adhesion) are introduced to quantify the extents of interface separation and adhesion, respectively. The interfaces in Fig. 6a,b are rendered in two damage variables, clearly indicating the separation between stainless-steel foils and the graphite layer and the adhesion between the graphite layer and lithium layer (more details in Supplementary Video 1), respectively. Furthermore, both experiments and FE simulations showed that only when the compressive strain induced by the rollers is greater than a critical value, a higher transfer-printing success rate can be achieved. In fact, the compression deformation induced by the rollers results in different shear and normal stresses around the interfaces, which dominate the interface separation and adhesion during the transfer-printing process[34]. We further performed a series of simulations to investigate the influence of the compressive strain on transfer-printing success rate. Figure 6c shows a phase diagram for compressive strain and transfer-printing success extent from FE simulations. It indicates that the higher compressive strain enables the easier transfer printing. However, it is noted that high shear and compressive stresses may damage the preGr electrode. It was found in our FE simulations that the compressive strain of 0.27 induces adequate shear and normal stresses, which cannot damage the preGr electrode and can ensure a relatively high success rate of transfer printing. To quantitatively characterize the separation between the stainless-steel and graphite electrode during transfer printing, we established a theoretical model for the compression of two-layer film (including the stainless-steel and graphite electrode) under a roller. Our theoretical model gave the following analytical expression of critical compressive strain for the separation between the stainless-steel and graphite electrode

$$\varepsilon_c = \frac{R}{h_0 + H}\left(\frac{T_t^0}{2\mu}\right)^2 \quad (1)$$

where R is the radius of the roller, h_0 is the thickness of graphite electrode, H is the thickness of other layers (including LiCF and stainless-steel foil), T_t^0 is the shear strength of the interface of the stainless steel and electrode and μ is the shear modulus of the electrode. More details of our theoretical model are given in Supplementary Methods (Supplementary Figs. 28–30). Figure 6d–f and Supplementary Fig. 31 show the influences of interfacial shear strength, thickness and modulus of electrode and radius of the roller on the critical compressive strain from our theoretical predictions and FE simulations.

https://doi.org/10.1038/s41560-023-01272-1

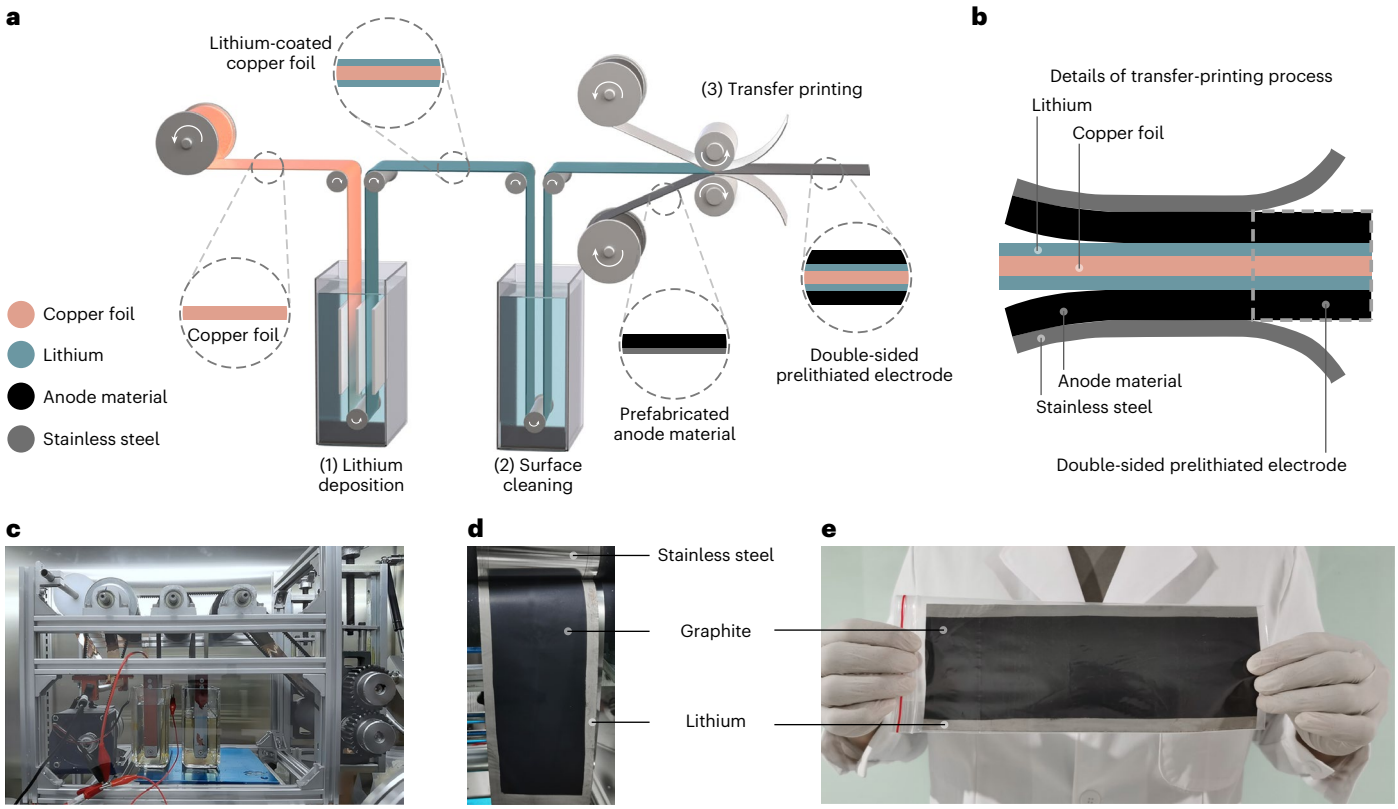

Fig. 7 | Roll-to-roll fabrication of transfer-printing anodes. a, Schematic illustration of our RET system. There are two baths in the RET system. From left to right: (1) the first bath is filled with electrolyte where lithium is deposited on copper foil; (2) the second bath is used to remove the residual electrolyte on copper foil. **b**, Sectional diagram illustration of our prelithiated electrode before and after transfer printing. **c**, Photograph of the RET system. The entire system is placed in an argon-filled glovebox (Supplementary Video 2). **d**, Transfer-printing process of the RET system. **e**, Photograph of prelithiated anode produced using the RET system.

It is seen in these figures that the predictions from our theoretical model are in good agreement with FE simulation results. A series of FE simulations for transferring on the double-sided electrode were performed and presented in Supplementary Figs. 32 and 33. It indicates that the single-sided or double-sided condition has no significant influence on the critical compressive strain for the separation between the stainless-steel and graphite electrode. Our FE simulations and theoretical model not only revealed the kinematic details of transfer printing during the roll-to-roll fabrication, the deformation behaviours and associated mechanisms of interface separation and adhesion but also provided a guide for subsequent experiments and industrial applications.

Roll-to-roll prelithiation

Through our FE simulations and theoretical model, the optimal conditions of transfer printing were worked out and used in a RET system for roll-to roll continuous production of prelithiated electrodes. Figure 7a shows a schematic illustration of the RET system. The RET system is composed of electrodeposition equipment, a surface-cleaning process system and a transfer-printing system. The copper foil typically undergoes the following three steps: first, electrodeposition of uniform lithium layers on both sides of the copper foil in the electrodeposition equipment; then, the cleaning of LiCF in the cleaning equipment; and finally, transfer printing of anode active material on both sides of the LiCF by calendering to produce double-sided prelithiated electrodes. Notably, similar techniques have been widely applied in flexible electronics for transferring solid objects from one substrate to another[35,36]. The anode active material can be coated on substrate foils or prepared as independent film electrodes.

After the transfer-printing process, the anode active material is peeled off from the substrate and closely integrated with the LiCF, and the substrate foil can be reused. Figure 7b shows the section-view diagram of the transfer-printing process. Figure 7c and Supplementary Video 2 demonstrates the working condition of the RET system. In this study, stainless-steel foils were used as substrates, and artificial graphite was selected as the anode material. Figure 7d presents the transfer-printing step of the RET system; the graphite layer on the GrSS is perfectly transferred onto the LiCF with no residue. Figure 7e shows a photograph of the double-sided prelithiated anode produced by the RET system. The electrode produced by the RET system can be easily applied to the following steps of battery assembly. Compared with similar prelithiation methods, this strategy offers notable advantages including lower costs and better industry adaptability with LIB manufacturing (Supplementary Table 2). Detailed information of the RET system is presented in the Supplementary Materials and Supplementary Fig. 34.

Conclusion

In this study, a transfer-printing process was developed to produce different types of prelithiated anode, and their applications for improving the energy density of LIBs were presented. Through FE simulations and theoretical modelling, it was revealed that interface separation and adhesion in the transfer-printing process are related to the interfacial shear stress and pressure, respectively, and thus a potential design with guiding significance was provided for subsequent experiments and industrial application. This prelithiation method guarantees ICEs of nearly 100% in both Gr and Si/C electrodes and stable SEI films, which benefit from the cyclic stability and rate capability in half cells. The prelithiated electrodes significantly enhance the ICEs and energy

density of full cells, when assembled with NCM and LFP cathodes. On the other hand, a low-cost and efficient RET system was further established herein for continuous production of prelithiated electrodes. This strategy can be universally applied to fabricate various electrodes and can perfectly link up with the current LIB industry.

Methods

Peeling experiment

To obtain the interface properties (the interface of the graphite layer and stainless steel and the interface of the lithium layer and graphite layer) used in simulations, a 90° peeling experiment is carried out in this work. As shown in Supplementary Figs. 23 and 24, all the experiments were performed using a universal testing machine (Bose3230) with effective capacity of 45 N and precision of 10 mN at a constant peeling rate of 0.6 mm s^{-1}. We use 3M vinyl electrical tape as thin film in the present experiment. To decrease the deviation of the peeling angle (90°) during the peeling process, a thin polyimide film with a length of about 30 cm connects one end of the 3M tape to the force sensor. Typical curves of the peeling force vs peeling distance are measured and presented in Supplementary Figs. 25 and 26. On the basis of the classical Kendall's model, for the 90° peeling experiment, we calculate the critical energy release rate of the interface by the following

$$G_{\text{interface}} = \frac{F_{\text{peeling}}}{w} \quad (2)$$

where $G_{\text{interface}}$ is the critical energy release rate of the interface for mode I (opening) interface fracture, F_{peeling} is the peel force and w is the width of the 3M tape.

Preparation of Gr and Si/C anodes

Gr anodes are prepared by blade coating the mixture of artificial graphite (MTI), carbon black (TIMCAL) and polyvinylidene fluoride (MTI) at a weight ratio of 8:1:1 in *N*-methyl-2-pyrrolidone (NMP). After blade coating on copper foil (10 µm thick), the Gr anodes were dried at 60 °C ambient air for 12 h and dried in a 120 °C vacuum for 12 h. The areal loading of graphite was about 3 mg cm^{-2}. Si/C anodes were prepared by blade coating the mixture of Si/C (CANRD), carbon black (TIMCAL), polyvinylidene fluoride (MTI) and polyacrylic acid (Aladdin, Mv ~450,000) at a weight ratio of 90:4:3:3 in *N*-methyl-2-pyrrolidone (NMP). After blade coating on copper foil, the Si/C anodes were dried in 60 °C ambient air for 12 h and dried in an 80 °C vacuum for 12 h. The areal loading of Si/C was about 4.5 mg cm^{-2}.

Preparation of LiCF, GrSS and prelithiation anodes

LiCF was prepared by lithium electrodeposition on the rough side of copper foil with a current density of 5 mA cm^{-2} in 1 M $LiPF_6$ in 1:1 (v/v) ethylene carbonate and dimethyl carbonate with lithium-foil anode in an argon-filled glovebox. The other side of the copper foil was protected by polyimide tapes. The electrodeposition time was determined by prelithiation degree. The LiCF was washed by dimethyl carbonate after electrodeposition. GrSS was by prepared by blade coating on stainless steel (30 µm thick) with the same slurry of Gr anode. After blade coating on stainless steel, the GrSS was dried in 60 °C ambient air for 12 h and in a 120 °C vacuum for 12 h before using. The areal loading of graphite was about 3 mg cm^{-2}. PreGr anodes were prepared by transfer printing using LiCF and GrSS in an argon-filled glovebox by a roller.

Roll-to-roll fabrication system

The roll-to roll fabrication system is driven by an alternating current dynamo. Copper foil (20 µm thick) is used as the current collector. 1 M $LiPF_6$ in 1:1 (v/v) ethylene carbonate and dimethyl carbonate was used as electrolyte in electrodeposition. Three pieces of lithium metal were used as anodes. Dimethyl carbonate was used as cleaning solvent. The current density is 5 mAh cm^{-2}.

Electrochemistry measurement

The half cells were assembled using CR-2025 cells with excess lithium-foil electrodes. The full cells were assembled using CR-2025 cells with NCM and LFP anodes. Graphite and Si/C anodes were cut into circles of 12 mm diameter and assembled in an argon-filled glovebox. Two layers of Celgard 2325 separators were used for separation. The electrolyte was composed of 1 M $LiPF_6$ in 1:1 (v/v) ethylene carbonate and diethyl carbonate with 1% vinylene carbonate and 10% fluoroethylene carbonate. For preventing harmful lithium plating and achieving better cyclic performance, the anode capacities were designed to be slightly higher than cathode capacities in these full cells. All the anodes were assembled with commercial NCM111 and LFP cathodes at an anode/cathode capacity ratio of 1.1.

NCM cathodes are prepared by blade coating the mixture of artificial NCM111 (MTI), carbon black (TIMCAL) and polyvinylidene fluoride (MTI) at a weight ratio of 90:5:5 in NMP. After blade coating on aluminium foil, the NCM cathodes were dried in 60 °C ambient air for 12 h and dried in 120 °C vacuum for 12 h. The areal loading of NCM was about 6 mg cm^{-2}. LFP cathodes are prepared by blade coating the mixture of artificial LFP (MTI), carbon black (TIMCAL) and polyvinylidene fluoride (MTI) at a weight ratio of 90:5:5 in NMP. After the blade coating on aluminium foil, the LFP cathodes were dried in 60 °C ambient air for 12 h and dried in a 120 °C vacuum for 12 h. The areal loading of LFP was about 6 mg cm^{-2}. The energy densities of these cells are calculated on active materials at 0.1C (additional lithium is taken into account).

Battery cycling data were collected using battery testers (LAND, 2001CT) at room temperature. Electrochemical tests were produced with an electrochemical workstation (CHI 660e). EIS measurements were performed by a potentiator with a frequency response analyser module (Metrohm Autolab). All the cells were at a state of charge of 50% before EIS measurements. The EIS measurements were conducted in the range of 100 kHz to 0.01 Hz at open-circuit potential. The CV curves were measured at a scan rate of 1 mV s^{-1}.

Characterization

The SEM images were taken by SEM (FESEM, Leo-1530). The samples contacted with the electrolyte were cleaned with dimethyl carbonate before observing. Raman spectra data were detected by laser Raman spectrometer (Evolution, HORIBA). XPS spectrum was detected by XPS (Escalab 250 xi, Thermo Fisher). XRD information was detected by XRD (D/max-2500/PC, Rigaku).

Data availability

All relevant data are contained in the manuscript, Supplementary Information, source data and https://doi.org/10.6084/m9.figshare.22672735. Source data are provided with this paper.

References

1. Schmuch, R., Wagner, R., Hörpel, G., Placke, T. & Winter, M. Performance and cost of materials for lithium-based rechargeable automotive batteries. *Nat. Energy* **3**, 267–278 (2018).
2. Li, M., Lu, J., Chen, Z. & Amine, K. 30 years of lithium-ion batteries. *Adv. Mater.* **30**, 1800561 (2018).
3. Su, X. et al. Silicon-based nanomaterials for lithium-ion batteries: a review. *Adv. Energy Mater.* **4**, 1300882 (2014).
4. Choi, J. W. & Aurbach, D. Promise and reality of post-lithium-ion batteries with high energy densities. *Nat. Rev. Mater.* **1**, 16013 (2016).
5. Kim, T., Song, W., Son, D.-Y., Ono, L. K. & Qi, Y. Lithium-ion batteries: outlook on present, future, and hybridized technologies. *J. Mater. Chem. A* **7**, 2942–2964 (2019).
6. Wood, D. L., Li, J. & Daniel, C. Prospects for reducing the processing cost of lithium ion batteries. *J. Power Sources* **275**, 234–242 (2015).

7. An, S. J. et al. The state of understanding of the lithium-ion-battery graphite solid electrolyte interphase (SEI) and its relationship to formation cycling. *Carbon* **105**, 52–76 (2016).
8. Zou, K. et al. Prelithiation/presodiation techniques for advanced electrochemical energy storage systems: concepts, applications, and perspectives. *Adv. Funct. Mater.* **31**, 2005581 (2021).
9. Sun, C. et al. Recent advances in prelithiation materials and approaches for lithium-ion batteries and capacitors. *Energy Storage Mater.* **32**, 497–516 (2020).
10. Sun, Y. et al. High-capacity battery cathode prelithiation to offset initial lithium loss. *Nat. Energy* **1**, 15008 (2016).
11. Wang, F. et al. Prelithiation: a crucial strategy for boosting the practical application of next-generation lithium ion battery. *ACS Nano* **15**, 2197–2218 (2021).
12. Forney, M. W., Ganter, M. J., Staub, J. W., Ridgley, R. D. & Landi, B. J. Prelithiation of silicon-carbon nanotube anodes for lithium ion batteries by stabilized lithium metal powder (SLMP). *Nano Lett.* **13**, 4158–4163 (2013).
13. Pan, Q. et al. Improved electrochemical performance of micro-sized SiO-based composite anode by prelithiation of stabilized lithium metal powder. *J. Power Sources* **347**, 170–177 (2017).
14. Wang, Z. et al. Application of stabilized lithium metal powder (SLMP®) in graphite anode—a high efficient prelithiation method for lithium-ion batteries. *J. Power Sources* **260**, 57–61 (2014).
15. Chen, H. et al. Free-standing ultrathin lithium metal–graphene oxide host foils with controllable thickness for lithium batteries. *Nat. Energy* **6**, 790–798 (2021).
16. Cao, Z. et al. Ambient-air stable lithiated anode for rechargeable Li-Ion batteries with high energy density. *Nano Lett.* **16**, 7235–7240 (2016).
17. Liu, N., Hu, L., McDowell, M. T., Jackson, A. & Cui, Y. Prelithiated silicon nanowires as an anode for lithium ion batteries. *ACS Nano* **5**, 6487–6493 (2011).
18. Kim, H. J. et al. Controlled prelithiation of silicon monoxide for high performance lithium-ion rechargeable full cells. *Nano Lett.* **16**, 282–288 (2016).
19. Saito, M., Osawa, M., Masuya, A. & Kawakatsu, K. Stabilization of Si negative electrode by Li pre-doping technique and the application to a new energy storage system. *Electrochemistry* **85**, 656–659 (2017).
20. Yan, Y. et al. High-safety lithium-sulfur battery with prelithiated Si/C anode and ionic liquid electrolyte. *Electrochim. Acta* **91**, 58–61 (2013).
21. Shen, Y. et al. Achieving desirable initial Coulombic efficiencies and full capacity utilization of Li-ion batteries by chemical prelithiation of graphite anode. *Adv. Funct. Mater.* **31**, 2101181 (2021).
22. Wang, G. et al. Chemical prelithiation of negative electrodes in ambient air for advanced lithium-ion batteries. *ACS Appl. Mater. Interfaces* **11**, 8699–8703 (2019).
23. Shen, Y., Qian, J., Yang, H., Zhong, F. & Ai, X. Chemically prelithiated hard-carbon anode for high power and high capacity Li-Ion batteries. *Small* **16**, 1907602 (2020).
24. Xu, H. et al. Roll-to-roll prelithiation of Sn foil anode suppresses gassing and enables stable full-cell cycling of lithium ion batteries. *Energy Environ. Sci.* **12**, 2991–3000 (2019).
25. Liu, Z. et al. A scalable cathode chemical prelithiation strategy for advanced silicon-based lithium ion full batteries. *ACS Appl. Mater. Interfaces* **13**, 11985–11994 (2021).
26. Ai, G. et al. Scalable process for application of stabilized lithium metal powder in Li-ion batteries. *J. Power Sources* **309**, 33–41 (2016).
27. Missyul, A., Bolshakov, I. & Shpanchenko, R. XRD study of phase transformations in lithiated graphite anodes by Rietveld method. *Powder Diffr.* **32**, S56–S62 (2017).
28. Andersen, H. L., Djuandhi, L., Mittal, U. & Sharma, N. Strategies for the analysis of graphite electrode function. *Adv. Energy Mater.* **11**, 2102693 (2021).
29. Didier, C., Pang, W. K., Guo, Z., Schmid, S. & Peterson, V. K. Phase evolution and intermittent disorder in electrochemically lithiated graphite determined using in operando neutron diffraction. *Chem. Mater.* **32**, 2518–2531 (2020).
30. Inaba, M. et al. In situ Raman study on electrochemical Li intercalation into graphite. *J. Electrochem. Soc.* **142**, 20–26 (1995).
31. Augustsson, A. et al. Solid electrolyte interphase on graphite Li-ion battery anodes studied by soft X-ray spectroscopy. *Phys. Chem. Chem. Phys.* **6**, 4185–4189 (2004).
32. Steinhauer, M., Risse, S., Wagner, N. & Friedrich, K. A. Investigation of the solid electrolyte interphase formation at graphite anodes in lithium-ion batteries with electrochemical impedance spectroscopy. *Electrochim. Acta* **228**, 652–658 (2017).
33. Giffith, A. A. VI. The phenomena of rupture and flow in solids. *Philos. Trans. R. Soc. A* **221**, 163–198 (1921).
34. Jang, H. W. & Kim, W. S. Shear-induced dry transfer of reduced graphene oxide thin film via roll-to-roll printing. *Appl. Phys. Lett.* **108**, 091601 (2016).
35. Eda, G., Fanchini, G. & Chhowalla, M. Large-area ultrathin films of reduced graphene oxide as a transparent and flexible electronic material. *Nat. Nanotechnol.* **3**, 270–274 (2008).
36. Meitl, M. A. et al. Transfer printing by kinetic control of adhesion to an elastomeric stamp. *Nat. Mater.* **5**, 33–38 (2006).

Acknowledgements

This work was supported by the Basic Science Center Program of the National Natural Science Foundation of China (NSFC) under grant number 52388201 (H.W.).

Author contributions

H.W. and X.L. conceived the idea and supervised the research. H.W. and C.Y. designed and constructed the experimental system. X.L. and H.M. performed the modelling and simulations. C.Y., R.Y., K.W., H.M., L.L. and F.X. synthesized the specimens and performed the analysis of different characterizations. C.Y., K.W., H.M., K.L., Y.L., H.Z., Y.Z., X.L. and H.W. contributed to writing the manuscript.

Competing interests

A patent (application number: CN202210508002.6, application date: 10 May 2022, patent status: under substantive examination) for the prelithiation method has been applied for on behalf of Tsinghua University. H.W., X.L. and C.Y. are listed as inventors. The invention discloses a prelithiated lithium-ion battery electrode and its preparation system, method and application, which correlated with the research. The other authors declare no competing interests.

Additional information

Supplementary information The online version contains supplementary material available at https://doi.org/10.1038/s41560-023-01272-1.

Correspondence and requests for materials should be addressed to Xiaoyan Li or Hui Wu.

Peer review information *Nature Energy* thanks K.H. Kim, Sandrine Lyonnard and the other, anonymous, reviewer(s) for their contribution to the peer review of this work.